Title
Parametric emittance measurements of electron beams produced by a laser plasma accelerator

Journal
Plasma Physics and Controlled Fusion, 60(5)

ISSN
0741-3335

Authors
Barber, SK
van Tilborg, J
Schroeder, CB
et al.

Publication Date
2018-05-01

DOI
10.1088/1361-6587/aab6cd

Peer reviewed

PAPER

Parametric emittance measurements of electron beams produced by a laser plasma accelerator

IOP Publishing Plasma Physics and Controlled Fusion
Plasma Phys. Control. Fusion **60** (2018) 054015 (8pp) https://doi.org/10.1088/1361-6587/aab6cd

Parametric emittance measurements of electron beams produced by a laser plasma accelerator

S K Barber[1], J van Tilborg[1], C B Schroeder[1], R Lehe[1], H-E Tsai[1], K K Swanson[1,2], S Steinke[1], K Nakamura[1], C G R Geddes[1], C Benedetti[1], E Esarey[1] and W P Leemans[1,2]

[1] Lawrence Berkeley National Laboratory, University of California, Berkeley, CA 94720, United States of America
[2] Department of Physics, University of California, Berkeley, CA 94720, United States of America

E-mail: sbarber@lbl.gov

Received 29 November 2017, revised 25 February 2018
Accepted for publication 15 March 2018
Published 4 April 2018

Abstract

Laser plasma accelerators (LPA) offer an exciting possibility to deliver high energy, high brightness electrons beams in drastically smaller distance scales than is typical for conventional accelerators. As such, LPAs draw considerable attention as potential drivers for next generation light sources and for a compact linear collider. In order to asses the viability of an LPA source for a particular application, the brightness of the source should be properly characterized. In this paper, we present charge dependent transverse emittance measurements of LPA sources using both ionization injection and shock induced density down ramp injection, with the latter delivering smaller transverse emittances by a factor of two when controlling for charge density. The single shot emittance method is described in detail with a discussion on limitations related to second order transport effects. The direct role of space charge is explored through a series of simulations and found to be consistent with experimental observations.

Keywords: laser plasma accelerator, high brightness, emittance, space charge, ionization injection, down ramp injection

(Some figures may appear in colour only in the online journal)

1. Introduction

Laser plasma accelerators (LPAs) [1] are being considered for applications ranging from a TeV scale linear collider [2] to drivers for 5th generation light sources [3–8]. To meet the requirements of these types of applications the LPA source must satisfy demanding brightness requirements, with the 6D electron beam brightness defined as $B_{6D} = Q/(\epsilon_x \epsilon_y \epsilon_z)$, where Q is the beam charge and $\epsilon_{x,y,z}$ are the normalized transverse and longitudinal emittances. As such, quantifying and parameterizing these emittances is critical to the success of future LPA based accelerator applications.

Unfortunately, the nature of LPA sources is such that standard techniques for measuring transverse and longitudinal emittances can be problematic. In the longitudinal domain the most robust means of measuring the longitudinal phase space relies on RF deflecting cavities [9]. However, achieving the fs scale resolution required for typical LPA sources with an RF deflector would require a cavity several meters in length and 10's of MW of power [10].

In the transverse domain large initial divergences coupled with significant energy spread lead to strong chromatic aberrations limiting the utility of standard single-shot techniques like pepper pot measurements [11]. Furthermore, LPA sources typically have poor shot-to-shot stability, which complicates the use of multi-shot scanning techniques like quadrupole scans. In light of these challenges, a number of indirect methods based on spectral analysis of x-ray betatron or Compton radiation have been used to measure transverse emittances of LPA sources [12–14]. These techniques,

however, rely on various assumptions, simulations, and complex analysis to unravel the e-beam source properties. A more direct and single-shot method was developed in [15]. With this technique, the electron beam is focused into a magnetic spectrometer and the energy resolved beam size is measured, resulting in something analogous to a quadrupole scan. Instead of varying the quadrupole strength, the natural energy spread of the source provides information on how the beam evolves as a function of energy through a fixed focusing system. With a well characterized and calibrated electron transport line, the initial transverse parameters of an the LPA source (over a a finite energy slice) can be readily deduced from this information. It should be noted that this method does rely on the assumption that the source emittance is not a function of energy over the bandwidth of interest.

We recently adopted this method to perform parametric emittance studies of LPA sources [16]. In particular, we presented a direct comparison of emittance measurements of electron beams generated by two different injection mechanisms: ionization injection [17–21] and shock-induced density down ramp injection [22–27]. Both schemes have attracted recognition as a path towards localized and controllable injection, and direct energy-dispersed emittance measurements were reported in [16].

A notable distinction between the two injection mechanisms is that in standard ionization injection the trapped electrons interact with the driving laser pulse in a non negligible way. That is, the eventually trapped electrons originate from ionization occurring near the peak of the laser intensity. The variation in times t_i at which the electrons are released relative to the peak of the laser and variation in the radial location relative to the propagation axis result in varying transverse ponderomotive kicks and varying residual transverse momentum in the laser polarization plane $p_\perp/m_e c \approx a(t_i)$ [28], with a the normalized laser strength. Both effects, which are absent in down ramp injection, lead to an increase of transverse emittance (particularly in the polarization plane). Thus, for an LPA being driven by the same laser, it might be anticipated that down ramp injection would produce beams of smaller transverse emittance compared to ionization injection.

This paper is organized in the following way. In section 2 we discuss the experimental setup, including some details on the two LPA configurations as well as a detailed discussion on the single-shot emittance diagnostic, including second order optics considerations. Results of the emittance measurements are discussed in section 3 followed by a section presenting full transport simulations to specifically examine how space charge affects these measurements. Finally, a short conclusion section is included.

2. LPA source and single-shot emittance diagnostic

A description of the experimental setup, which is briefly reviewed here, can be found in [16, 27]. The drive laser used is a multi-terawatt Ti:sapph laser that delivers 1.8 J on target. The target itself consists of a supersonic gas jet which can deliver either pure hydrogen for the down ramp injection scheme or a mixture of 99% helium and 1% nitrogen for the ionization injection scheme. In order to create the density drop necessary to allow down ramp injection, an adjustable thin blade is used to block a portion of the gas jet thereby creating a strong density drop in the gas flow. To make a fair comparison between the two injection mechanisms, it is necessary to ensure beams of comparable central energy are produced using the two methods. The energy of the beam generated by down ramp injection is easily controlled by adjusting the blade position relative to the gas jet, which effectively adjusts the total accelerator length. The central energy of the beam generated via ionization injection is controlled by introducing small transverse offsets of the gas jet, thereby controlling the length of the plasma through the laser propagates. In this way, e-beams with central energies of 57 MeV were produced with both injection mechanisms.

The transport line for the generated electron beam was carefully designed to allow direct, single-shot emittance measurements using the method mentioned in the introduction. The key components were a permanent magnet quadrupole (PMQ) triplet combined with a magnetic spectrometer dipole. A triplet configuration of the quadrupoles was chosen for the benefit of symmetric focusing which aids in minimizing potential resolution limits, as is discussed in subsequent paragraphs. With a 1 inch bore, the individual quadrupoles produce relatively modest field gradients of 50 $\mathrm{T\,m^{-1}}$. At the same time, however, the large aperture allows excellent field quality near the central axis. Details of the specific PMQ triplet used in this experiment, which was fabricated by Radiabeam Technologies, are documented in [29]. It should be noted that in [29] this triplet was used to focus an incoming electron beam which was nearly collimated. In the context of the present experiment, rather than focus a collimated beam, the PMQ triplet is used to magnify the generated LPA beam. Accordingly, the triplet is oriented in a reversed configuration compared to [29]. After magnification with the PMQ triplet, the beam is energy dispersed by the magnetic spectrometer. The beam is then incident upon a 300 μm thick scintillating Ce:YAG crystal which is imaged by a CCD camera equipped with a long working distance microscope objective providing 8 μm optical resolution. A schematic of the experimental setup, along with an example spectrometer image is shown in figure 1.

From a measurement of the energy resolved beam size, the vertical emittance can be readily deduced using standard linear charged particle beam optics [15, 16, 30]. The vertical beam size at each energy is a function of the 6 × 6 transfer matrix, **R**, and the initial source properties of the beam:

$$\sigma_y(E) = \sqrt{[R_{34}(E^*)]^2(\epsilon_y/\gamma\sigma_{y0})^2 + [R_{33}(E^*)]^2\sigma_{y0}^2}, \quad (1)$$

where $E^* = E - \Delta E$, and γ is the relativistic Lorentz factor. The transfer matrix **R** represents the total transformation of the beam from source to diagnostic screen and is a product of all the drifts, quadrupoles and dipoles in the transport line. In this convention, the indices of the **R** matrix refer to the coordinates $\{x, x', y, y', z, \delta\}$, where $\delta = \delta p_z/p_0$ is the momentum deviation. Thus, the R_{34} term relates the initial

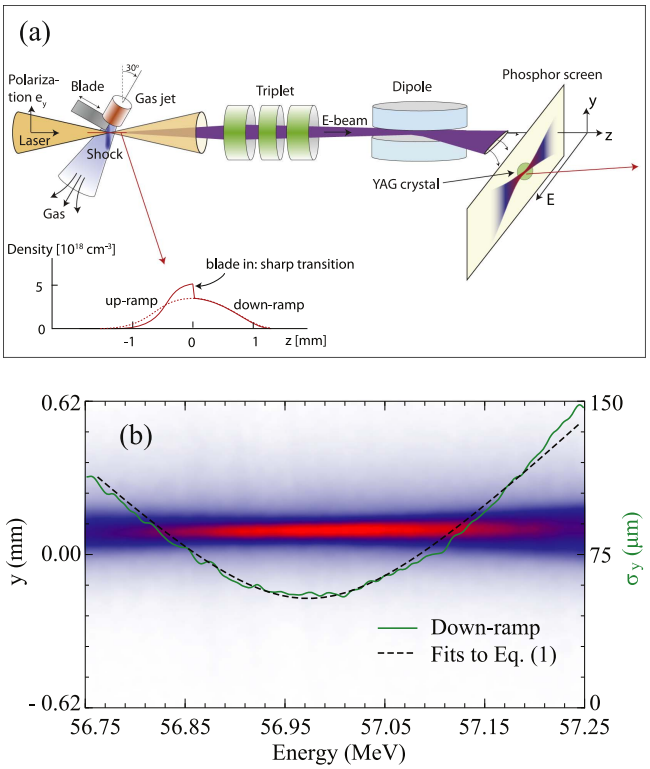

Figure 1. (a) Depiction of experimental setup. A multi TW laser pulse is focused on a supersonic gas jet generating electrons. A PMQ triplet located downstream images the source onto a scintillating YAG screen. Between the YAG screen and PMQ triplet, a magnetic spectrometer disperses the beam in the horizontal plane providing a means to measure the energy resolved vertical beam size. (b) An example image of the focused and energy dispersed beam. The measured beam size along with a fit of the beam size to equation (1) are overlaid and shown in the green and black dashed lines respectively.

vertical divergence to the final vertical beam size. Consequently, point-to-point imaging is achieved when $R_{34} = 0$. Likewise, the R_{33} term is equivalent to the vertical spatial magnification of the beam. Because the effective focusing strength of a quadrupole has a natural dependence on the particle energy, the transfer matrix itself has an energy dependence, which is included in equation (1). It should be noted that in general there may exist a correlation between y and y' in the initial phase space of the beam, which would result in an additional term under the square root of equation (1) that is proportional to the the product of R_{33} and R_{34}. However, a correlation of this type results simply in a shift of the $\sigma_y(E)$ curve along the E axis. Thus, this correlation term is accounted for in the description of $\sigma_y(E)$ with the inclusion of the ΔE term. Formulating $\sigma_y(E)$ in this way also allows for a means of identifying the influence of space charge, as is discussed in a subsequent section. With a well characterized transport line the transfer matrix $\mathbf{R}$ and its energy dependence are known allowing equation (1) to be fit to measured $\sigma_y(E)$ curves using the free parameters ϵ_y, σ_{y0} and ΔE.

The discussion up to this point has only included first order optics, in which the e-beam transport is fully described by the 6×6 $\mathbf{R}$ matrix. For completeness, we also consider second order contributions to $\sigma_y(E)$. In a standard notation, the second order transport elements are represented by the $6 \times 6 \times 6$ tensor with elements T_{ijk} [31]. In the context of LPA sources, it is primarily the terms which couple to the large initial divergences and energy spreads that can have a non negligible effect. In fact, in the context of this particular transport line, the dominant second order contribution to $\sigma_y(E)$ comes from the T_{346} element, which couples to the initial vertical divergence and energy spread (in the case at hand, it is actually the energy dependent spectrometer resolution that should be considered, rather than the integrated energy spread). Including this second order contribution, $\sigma_y(E)$ can be written as

$$\sigma_y(E) = \{[R_{33}(E^*)]^2\sigma_{y0}^2 + ([R_{34}(E^*)]^2 + [T_{346}(E^*)]^2[\delta(E^*)]^2)(\epsilon_y/\gamma\sigma_{y0})^2\}^{\frac{1}{2}}, \quad (2)$$

where $\delta(E)$ represents the energy dependent spectrometer resolution which can be expressed as $\delta(E) = \sqrt{\beta_x(E)\epsilon_x/\gamma}/\eta_x$. In this last expression, $\beta_x(E)$ is the horizontal Twiss beta function, ϵ_x is the normalized horizontal emittance and η_x is the horizontal dispersion. It should be noted that the expression $\sqrt{\beta_x(E)\epsilon_x/\gamma}$ is simply the dispersion free horizontal beam size $\sigma_x(E)$, which can be expressed in an analogous form to equation (1), with the matrix elements R_{33} and R_{34} being replaced by R_{11} and R_{12}, respectively. Second order contributions to $\sigma_y(E)$ are minimized when the waists for $\sigma_y(E)$ and $\sigma_x(E)$ [or equivalently, $\delta(E)$] are overlapped. In other words, the imaging condition should be satisfied in both planes for the same energy: $R_{12}(57) = R_{34}(57) = 0$. This ensures the relative contribution to $\sigma_y(E)$ from second order effects is minimized. The transport line for this experiment was designed to satisfy these conditions and is thus relatively insensitive to second order contributions.

In practice, however, it can be difficult to verify the lattice is optimized as intended. That is, the magnetic spectrometer disperses the electron beam in the horizontal plane making it straightforward to find the minimum of $\sigma_y(E)$ but not the minimum of $\sigma_x(E)$. We therefore have to rely on a well designed and characterized lattice to ensure mitigation of second order aberrations. While verifying that $\sigma_y(E)$ is minimized at the design energy of 57 MeV provides a good benchmark for the optics, the influence of some imperfections or errors in the lattice should be considered. As an example, we consider the effect of shifting the entire PMQ triplet by 1 cm downstream. Figure 2(a) shows plots of $\sigma_y(E)$ and $\delta(E)$ for both the optimal lattice configuration and shifted triplet configuration. A source with very small emittance and large divergence is chosen to illustrate the effect. In the optimal configuration (solid lines), $\delta(E)$ is minimized right at 57 MeV, along with $\sigma_y(E)$, resulting in a minimum vertical beam size of less than 10 μm. With the triplet shifted (dashed lines), the waists of $\sigma_y(E)$ and $\delta(E)$ separate leading to much poorer spectral resolution at the waist of $\sigma_y(E)$. This degraded

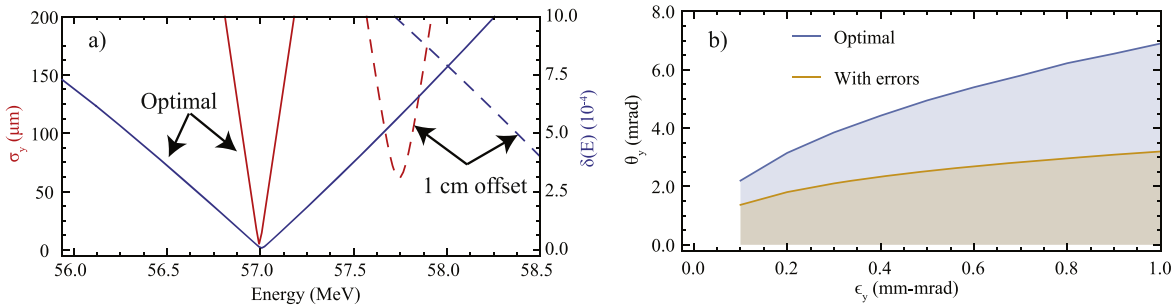

Figure 2. (a) Plots of $\sigma_y(E)$ and $\delta(E)$ for the optimal lattice configuration (solid lines) and in a configuration with the PMQ triplet shifted downstream by 1 cm (dashed lines). (b) Parameter space over which fitting to the linear model is accurate to better than 20% (represented by the shaded areas) for the design lattice (blue shaded region) and a lattice with errors representative of the uncertainty in our experiment (yellow shaded region).

resolution coupled to T_{346} becomes the dominate contributor to the waist size of $\sigma_y(E)$. Fitting the $\sigma_y(E)$ curve for this non optimal configuration with the first order equation (equation (1)) results in significant overestimate of the emittance. On the other hand, fitting $\sigma_y(E)$ from the optimal configuration with the linear model would still give an accurate estimate of the emittance.

In order to understand the accuracy limits of this emittance diagnostic we performed a series of particle tracking simulations in which particles are tracked from the source to the YAG screen location downstream of the spectrometer. The energy resolved beam size $\sigma_y(E)$ is calculated from the projected distribution and using equation (1), a least squares fit is performed to estimate the emittance, which is then compared to the initially chosen value. We considered two different scenarios: (i) the design lattice which is optimized to minimize second order contributions and (ii) a lattice with small errors relative to the design lattice. The errors considered here include, for example, small variations in the drift lengths. It should be noted, however, that the values for R_{33} and R_{34} in equation (1) always represent the error free design lattice. The primary effect of lattice errors is to make the $\sigma_y(E)$ curve more susceptible to second order aberrations. The end result is that with lattice errors, combined with second order aberrations, a fit of the $\sigma_y(E)$ curve using equation (1) with the design values for R_{33} and R_{34} will result in an over estimate of the emittance. Furthermore, even in the error free case, second order contributions impose limits on the smallest emittance that can be accurately resolved with this measurement technique. With these particle tracking simulations, we are able to estimate these limits for both the error free case (i) and the non ideal case (ii). In the non ideal case, we consider errors relative to the design lattice which are commensurate with the level of uncertainty in our experimental setup. In figure 2(b) the results of these simulations are distilled into a single plot which illustrate the parameter space over which this emittance measurement method can be considered accurate. For this plot we have defined an accuracy limit of 20%. That is, the shaded areas represent the parameter space over which the emittance value determined by a fit of the simulated $\sigma_y(E)$ to equation (1) is accurate to better than 20% with the blue and yellow areas corresponding to the design case and the non ideal lattice, respectively.

From this analysis we can draw an approximate condition for which our emittance diagnostic is accurate to better than 20% even in the presence of uncertainty in the lattice: $\sigma_{y'0}$ (mrad) $\lesssim 1.5 + 2.0\epsilon_y$ (mm mrad). The condition for the optimized design lattice is more relaxed. It should also be noted that the lattice errors and second order optics discussed here introduce a systematic error as it relates to the emittance determination. As such, it does not adversely the cross comparison of the two injection methods, nor the measured charge dependences.

3. Measured emittance dependence

Single-shot emittance measurements were taken using both injection methods, with at least 75 shots taken for each configuration to collect statistics. The first step in quantifying the emittance is to determine the beam size at each energy slice from the recorded images. The existence of tails in the individual profiles tends to limit the utility of the full rms beam size. Accordingly, we ascertain the beam size by applying a threshold at 50% of the peak value and fitting the remaining core of the profile to a Gaussian function with the form $e^{-y^2/2\sigma_y^2}$. For the vast majority of the data, the central peak (above the 50% threshold) of the profile is well described by Gaussian. It should also be noted that when reporting charge (or charge density) for a given emittance, we include only the charge which is encompassed by the Gaussian fit, and exclude the charge in the tails. In this sense, we are reporting the emittance of a core part of the beam. The choice of this beam size determination is further motivated by noting that space charge effects can also lead to the existence of tails (as is discussed in the next section) and thus may not be entirely representative of the source itself.

These measurements, which were first presented in [16], are shown in figure 3(a). Notable results include measured emittances as small as 0.5 mm mrad and a clear distinction between the two injection schemes with down-ramp injection significantly outperforming ionization injection when controlling for charge

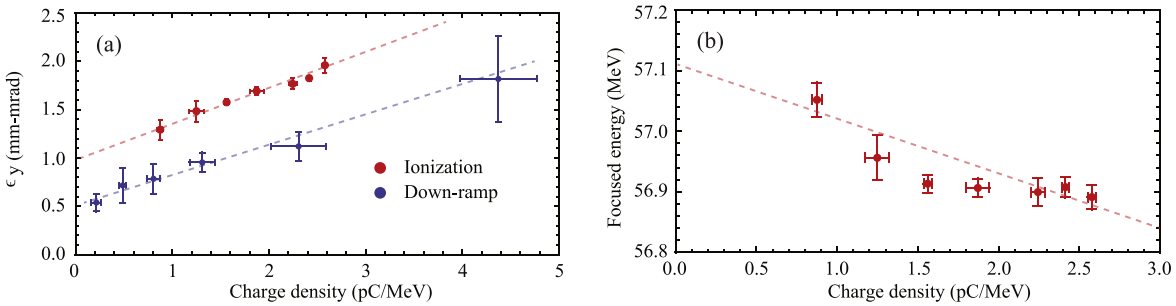

Figure 3. (a) Measured emittance dependence on spectral charge density for ionization injection (red) and down-ramp injection (blue). (b) Shift of the focused energy related to the ΔE fit parameter. Dashed lines in both figures are to provide a guide for the eye.

density. Interestingly, there is correlation between the focused energy, which is related to the ΔE fit parameter, and charge density, figure 3(b). As is mentioned in [16], with relatively low energy of the accelerated beam and significant accelerated charge, space charge likely played a role in the charged particle dynamics that can affect the measured properties. The trend observed in figure 3(b) is evidence of such an effect.

4. Space charge considerations

To understand the effects of space charge in the context of this experiment we performed a series of space charge simulations using the Astra package [32]. For each simulation, macro-particle distributions are tracked from the LPA source all the way to the diagnostic YAG screen location and the projected transverse distributions are analyzed using the same method as the actual measurements. Examples of simulated profiles with and without space charge effects included, along with the energy dependent vertical beam size (red lines), are shown in figure 4. In this example, both a shift in the waist location of $\sigma_y(E)$ towards lower energy and an increase in the minimum size of $\sigma_y(E)$ in the presence of space charge are clearly illustrated. The shift in the focused energy is explained by the fact that the inclusion of space charge effects in the description of the transverse dynamics of the electron beam adds a defocusing term proportional to the generalized perveance, $K = I_b/I_A\beta^3\gamma^3$, where I_b is the beam current, $I_A \approx 17$ kA is the Alfvén current, and β and γ are the relativistic factors. This effective reduction in focusing strength causes a shift of the apparent focused energy towards lower energies when space charge is included. The degree to which the focus is shifted depends on K, a trend which is noted in the data, figure 3(b). The increase in the minimum beam size in figure 4(c) is indicative of an increase in emittance.

In analyzing these simulated distributions, it was noted that the charge profile at a given energy E tends to become non Gaussian in the presence of space charge; the profiles can develop tails as is shown in figure 4(d). Tails like this were also observed in the measurements [33]. While this might be taken as an indication of space charge effects evident in the measurements, the existence of tails can also be a property inherent to the source. In order to more directly relate the simulations to measurements we apply the same thresholding and Gaussian fit routine discussed in section 3 to determine the beam size at each energy slice.

The difficulty in quantifying the space charge effects in the measurements lies in the fact that such effects are sensitive to the specifics of the detailed properties of the longitudinal phase space, which are not simultaneously measured. As an example, we consider the effect of varying the initial bunch length while the remaining initial properties of the source remain fixed. The simulated LPA source beam is initially Gaussian in the transverse dimensions and momentum deviation with 15 pC total charge, 57 MeV central energy and 2.5% rms energy spread. The current profile is taken to be flat top with total length L_b and is varied from 5 to 12.5 μm. For the transverse properties, we consider two configurations: (i) $\epsilon_{x,y} = 0.3$ mm mrad and $\sigma_{x,y} = 1.6$ μm and (ii) $\epsilon_{x,y} = 0.6$ mm mrad and $\sigma_{x,y} = 3.2$ μm. For these two transverse configurations the beam is taken to be at a waist and the source divergences are the same. Results of these simulations are shown in figure 5. Again, the emittance is determined by fitting each final $\sigma_y(E)$ to equation (1). For the low emittance case, the growth is particularly bad, and even at $\epsilon_{x,y} = 0.6$ mm mrad the growth can be as much as 50%. These simulations do of course indicate that the emittance growth is strongly related to the initial emittance. Importantly, the final emittance also has a notable dependence on the initial bunch length for both initial emittances.

Because of this sensitivity to the initial bunch length, it is difficult to completely decouple space charge effects from the intrinsic LPA source properties in the data. Nonetheless, valuable insight can still be obtained by examining the role of space charge on sources with initial parameters consistent with what was measured, i.e. charge, energy spread, emittance. To perform such a study, we consider a source with $\epsilon_{x,y} = 0.5$ mm-mrad that is initially at a waist with $\sigma_{x,y} = 2.1$ μm. The central energy is 57 MeV with 5.0% rms energy spread. These numbers are chosen to correspond the measured 'space charge free' LPA source generated by down ramp injection. For the current profile we assume a flat top distribution and consider several reasonable values which satisfy $L_b < \lambda_p$, where L_b is the total bunch length and λ_p is the plasma wavelength which is on the order of 20 μm for the plasma densities used in this experiment. The total charge in the bunch is varied in the range of 1–100 pC which serves to cover the range of spectral charge densities observed experimentally and it also covers a range in which space charge is negligible. Results of these simulations are shown in figure 6, with several notable results. First, as the charge in the bunch is increased the emittance clearly begins to

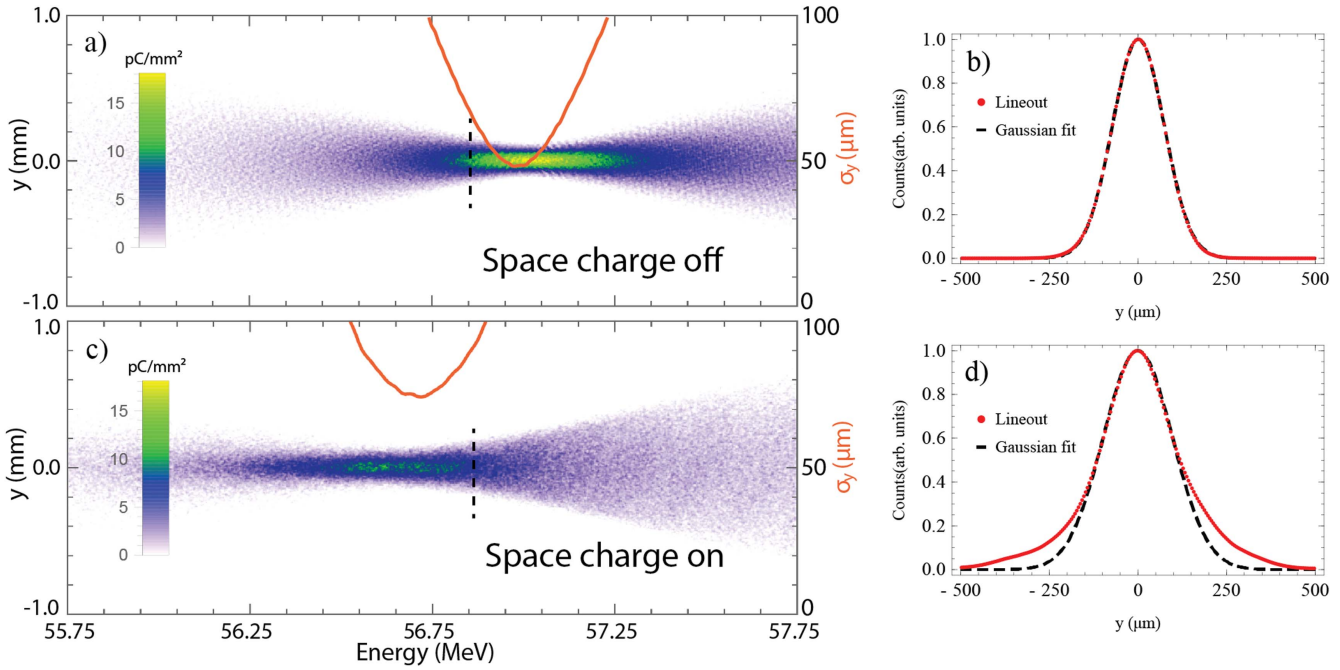

Figure 4. Simulated measurements using the space charge and particle tracking software Astra [32] demonstrating the effect of space charge. Initial beam parameters are $Q = 15$ pC, $E_0 = 57$ MeV, $\delta p/p = 2.5\%$, $L_b = 7.5$ μm, $\epsilon_{x,y} = 0.6$ mm-mrad, and $\sigma_{x,y} = 3.2$ μm. The images in (a) and (c) are projections of the particle distributions in the x–y plane at a location corresponding the YAG screen diagnostic. The horizontal axis (x axis) is converted to energy based on the properties of the magnetic spectrometer. With space charge turned on, the waist location of $\sigma_y(E)$ shifts towards lower energies and the minimum beam size is significantly increased. Profile lineouts (b) and (d) taken along the black dashed lines in (a) and (c) along with Gaussian fits.

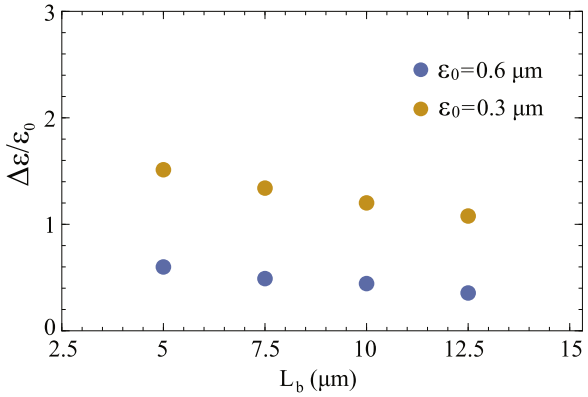

Figure 5. Simulated space charge induced emittance growth as a function of initial bunch length for an LPA source with 10 pC of charge, 2.5% rms energy spread.

grow, as shown in figure 6(b). How much and how quickly the emittance grows depends on the bunch length. For the long bunch case $L_b = 15$ μm (green line), the emittance increases only very slightly, where as for the $L_b = 7.5$ μm case (yellow line), it grows by almost a factor of 2 to $\epsilon_y = 1.0$ mm-mrad at the highest charge density. The focused energy (the energy at which $\sigma_y(E)$ is a minimum) exhibits a trend of shifting to lower energies with increasing charge, as shown in figure 6(b). Again, the larger the charge density, the more rapidly the focus shifts. In fact, the focus shift appears to exhibit a dependence roughly proportional to the generalized perveance K, consistent with the explanation given at the beginning of this section.

The qualitative results of these simulations are perhaps unsurprising. That the emittance would grow and that the beam would defocus with increasing charge might be easily predicted. However, the amplitude of the emittance growth and focused energy shift is harder to predict, and in comparing the simulation results to the data in figure 3 there are notable similarities. In particular, the magnitude of the focused energy dependence on charge density observed in figure 3(b) is well reproduced by the simulations, with the best agreement with data occurring for the simulated case $L_b = 7.5$ μm. That the magnitude of the focused energy shift produced in simulations matches what was observed in the measurements suggests space charge is playing a role.

In terms of the emittance dependence on charge density, it is notable that even for the shortest bunch length in the simulations the space charge induced emittance growth does not fully account for what was measured. That is, for $L_b = 3.75$ μm the space charge simulations predict roughly 50% less emittance growth than what was observed for the down ramp injection measurements. Most likely this is related to the LPA source itself. In the simulations, the emittance of the source is taken to be constant for all charges, while in reality it is likely that the LPA source emittance itself has some dependence on charge. Larger emittances were measured compared to the simulations suggesting the measurements are indeed tied to the LPA source itself and not space charge dominated. Still, it is likely that space charge does degrade the emittance to some extent in the transport from LPA source to the diagnostic screen. This implies the

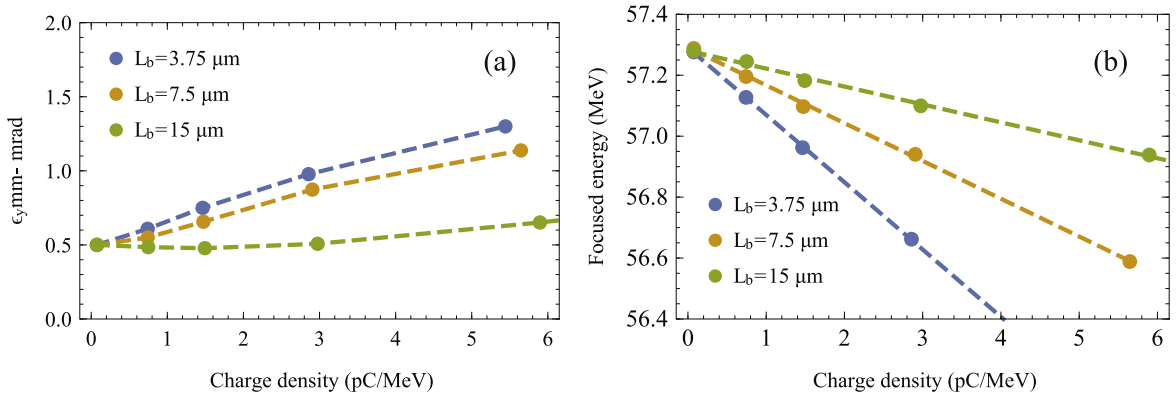

Figure 6. Results of space charge simulations showing (a) the emittance determined by fitting the $\sigma_y(E)$ to equation (1) and (b) the focused energy shift. Initial source parameters are chosen to be consistent with measured values.

LPA source has an initially higher brightness than what is determined by these measurements.

It should be emphasized that these simulations only encapsulate a subset of possible variations in the experimental parameter space. As such, the relative consistency between the simulations and measurement data should not be taken as a means of determining bunch length, for example. Such a prediction would require more details on the initial properties of the beam, beyond those that were measured. Rather, with these exploratory simulations we have substantiated predictions that space charge is likely playing an important role in the context of this experiment.

5. Conclusion

A dedicated single-shot transverse emittance measurement setup was implemented on an LPA beamline to parameterize the source emittance on both charge and injection mechanism. In particular, two injection schemes were employed: ionization induced injection and shock induced density down ramp injection. The measured emittances for both injection methods display linear dependence on the spectral charge density with down ramp out performing ionization injection by roughly a factor of two. A discussion of the emittance measurement method is examined in detail and resolution limits related to second order optics are identified. In accordance with these limits, the transport line was specifically designed to minimize second order contributions. The role of space charge in the context of the experiment was examined through a series of simulations. Even without detailed information on the longitudinal profile, the simulations provide good context for understanding the measurements and signatures of space charge are identified in the simulations which are also present in the data. Furthermore, in a quantitative sense, the simulations produce results which are consistent with what was measured.

Acknowledgments

This work was supported by the US Department of Energy (DOE) under Contract No. DE-AC02-05CH11231, by the National Science Foundation under Grant No. PHY-1415596 and PHY-1632796, by the US DOE National Nuclear Security Administration, Defense Nuclear Non-proliferation R&D (NA22), and by the Gordon and Betty Moore Foundation under Grant ID GBMF4898.

ORCID iDs

S K Barber https://orcid.org/0000-0001-7251-8755
K Nakamura https://orcid.org/0000-0001-9842-7114

References

[1] Esarey E, Schroeder C B and Leemans W P 2009 *Rev. Mod. Phys.* **81** 1229–85
[2] Schroeder C B, Esarey E, Geddes C G R, Benedetti C and Leemans W P 2010 *Phys. Rev. Spec. Top. Accel. Beams* **13** 101301
[3] Nalkajima K 2008 *Nat. Phys.* **4** 92–3
[4] Maier A R, Meseck A, Reiche S, Schroeder C B, Seggebrock T and Grüner F 2012 *Phys. Rev.* X **2** 031019
[5] Huang Z, Ding Y and Schroeder C B 2012 *Phys. Rev. Lett.* **109** 204801
[6] Couprie M E *et al* 2016 *Plasma Phys. Control. Fusion* **58** 034020
[7] Hajima R, Kikuzawa N, Nishimori N, Hayakawa T, Shizuma T, Kawase K, Kando M, Minehara E, Toyokawa H and Ohgaki H 2009 *Nucl. Instrum. Methods* A **608** S57–61
[8] Tesileanu O, Ursescu D, Dabu R and Zamfir N V 2016 *J. Phys.: Conf. Ser.* **420** 012157
[9] Emma P J, Frisch J and Krejcik P *Report No.* LCLS-TN00-12
[10] Dolgashev V A, Bowden G, Ding Y, Emma P, Krejcik P, Lewandowski J, Limborg C, Litos M, Wang J and Xiang D 2014 *Phys. Rev. Spec. Top. Accel. Beams* **17** 102801
[11] Cianchi A *et al* 2013 *Nucl. Instrum. Methods* A **720** 153–6
[12] Kneip S *et al* 2012 *Phys. Rev. Spec. Top. Accel. Beams* **15** 021302
[13] Plateau G R *et al* 2012 *Phys. Rev. Lett.* **109** 064802
[14] Golovin G *et al* 2016 *Sci. Rep.* **6** 24622
[15] Weingartner R *et al* 2012 *Phys. Rev. Spec. Top. Accel. Beams* **15** 111302
[16] Barber S K *et al* 2017 *Phys. Rev. Lett.* **119** 104801
[17] McGuffey C *et al* 2010 *Phys. Rev. Lett.* **104** 025004
[18] Chen M, Sheng Z M, Ma Y Y and Zhang J 2006 *J. Appl. Phys.* **99** 056109

[19] Chen M, Esarey E, Schroeder C B, Geddes C G R and Leemans W P 2012 *Phys. Plasmas* **19** 033101
[20] Pak A, Marsh K A, Martins S F, Lu W, Mori W B and Joshi C 2010 *Phys. Rev. Lett.* **104** 025003
[21] Clayton C E *et al* 2010 *Phys. Rev. Lett.* **105** 105003
[22] Bulanov S, Naumova N, Pegoraro F and Sakai J 1998 *Phys. Rev.* E **58** R5257–60
[23] Geddes C G R, Nakamura K, Plateau G R, Toth C, Cormier-Michel E, Esarey E, Schroeder C B, Cary J R and Leemans W P 2008 *Phys. Rev. Lett.* **100** 215004
[24] Schmid K, Buck A, Sears C M S, Mikhailova J M, Tautz R, Herrmann D, Geissler M, Krausz F and Veisz L 2010 *Phys. Rev. Spec. Top. Accel. Beams* **13** 091301
[25] Gonsalves A J *et al* 2011 *Nat. Phys.* **7** 862–6
[26] Buck A *et al* 2013 *Phys. Rev. Lett.* **110** 185006
[27] Swanson K K *et al* 2017 *Phys. Rev. Accel. Beams* **20** 051301
[28] Schroeder C B, Vay J L, Esarey E, Bulanov S S, Benedetti C, Yu L L, Chen M, Geddes C G R and Leemans W P 2014 *Phys. Rev. Spec. Top. Accel. Beams* **17** 101301
[29] Fedurin M, Babzien M, Yakimenko V, Allen B, Muggli P and Murokh A 2012 *Proc. IPAC'12 (New Orleans, USA, May 2012)* paper MOP057 2753
[30] Vafaei-Najafabadi N *et al* 2016 *Plasma Phys. Control. Fusion* **58** 034009
[31] Carey D C 1987 *The Optics of Charged Particle Beams* (New York: Harwood Academic)
[32] Floettmann K ASTRA
[33] van Tilborg J, Barber S K, Benedetti C, Schroeder C B, Isono F, Tsai H E, Geddes C G R and Leemans W P 2018 *Phys. Plasmas* **25** 056702